

Change in Microstructure of Selectively Laser Melted AlSi10Mg Alloy with Heat Treatments

Naoki Takata*, Hirohisa Kodaira**, Keito Sekizawa**, Asuka Suzuki,
Makoto Kobashi

Department of Materials Process Engineering, Graduate School of Engineering,
Nagoya University, Furo-cho, Chikusa-ku, Nagoya, 464-8603 Japan

* Corresponding author,

E-mail address: takata.naoki@material.nagoya-u.ac.jp

** Graduate student

Keywords:

Additive manufacturing; Porous metal; Aluminum alloy; Microstructure; Electron back-scattered diffraction pattern (EBSD)

Abstract

In the present study, we examined changes in the microstructure and mechanical properties of AlSi10Mg alloy, initially fabricated using selective laser melting (SLM) combined with a powder-bed system, by applying heat treatments at temperatures of either 300 or 530 °C. The as-fabricated samples exhibited a characteristic microstructural morphology and {001} texture. Melt pools corresponding to the locally melted and rapidly solidified regions were found to be composed of several columnar α -Al grains surrounded by fine eutectic Si particles. A fine dislocation substructure consisting of low-angle boundaries is present within the columnar α -Al grains. At elevated temperatures, fine Si phase precipitates within the columnar α -Al phase and coarsening of the eutectic Si particles occurs. These fine Si particles inhibit grain growth in the α -Al matrix, resulting in the microstructural morphology and [001] texture observed in the heat-treated samples. The dislocation substructure disappears in the columnar α -Al grains. Furthermore, the formation of a stable intermetallic phase occurs, reaching microstructural equilibrium after long-term exposure. The as-fabricated specimen exhibits a high tensile strength of approximately 480 MPa. The strength is independent of the tensile direction, that is, normal and parallel to the building direction. In contrast, the tensile ductility is found to be direction-dependent, and is therefore responsible for a fracture preferentially occurring at a melt pool boundary. The direction-dependence of the tensile ductility was not found in the specimen that had been heat-treated at 530 °C. The present results provide new insights into the control of the direction-dependence of the tensile properties of AlSi10Mg alloys fabricated by SLM.

1. Introduction

Porous materials can present unique physical properties like a low apparent density, a high impact-energy absorption, low thermal conductivity, gas permeability, and a high specific stiffness [1–5]. This endows these materials with a wide range of potential applications in the areas of thermal insulation, shock damping/absorption, acoustic absorption, catalyst support, and biomedical implants. Porous aluminum (Al) alloys have been intensively studied [6,7] in terms of their compressive absorption properties and simple production process. These porous Al alloys have attracted considerable attention due to their deformability and low density, making them promising candidates for application to the crumple zones of automobiles [3]. To improve the energy absorption capability of such alloys, it is necessary to control the factors affecting the porous structure, such as the porosity, pore size, pore shape, and pore distribution.

One potential processing route for fabricating open-cell porous materials with a controlled porous structure is powder bed fusion (PBF) additive manufacturing [8]. Powder bed fusion processes use either laser or electron beams to melt and fuse powdered metals and/or alloys. These processes include the commonly used selective laser melting (SLM), selective laser sintering (SLS), direct metal laser sintering (DMLS), electron beam melting (EBM), and selective heat sintering (SHS) [9,10]. New technological developments have recently been applied to the SLM process [9,10] to enable the fabrication of cellular lattice structures using a range of metals and alloys [11]. A porous Al alloy with a cellular lattice structure fabricated by SLM exhibits an unstable compressive stress with a series of peaks and troughs [12,13]. These compressive properties cannot satisfy the requirements of the structural parts of crumple zones, since this application requires a stable and highly reliable compressive strength (plateau-stress) to achieve high energy absorption [7]. Preliminary experiments revealed that subsequent heat treatments influence the deformation behavior of porous Al alloys fabricated by SLM, leading to a more stable deformation under compression. These results give rise to the possibility of fabricating a porous Al alloy with superior impact energy absorption

through the application of the SLM process together with additional heat treatments. To optimize the compressive properties by the application of heat treatment, it is essential to understand the development of the microstructures of Al alloys fabricated by SLM during the heat treatment, together with the associated mechanical properties. However, most previous studies have focused on the effect of T6 heat treatments (solution treatment and subsequent aging) on the mechanical properties of Al alloys fabricated by SLM [14–16] since AlSi10Mg alloy (the most commonly used alloy for additive manufacturing [17]) is recognized as being an age-hardenable alloy. Therefore, the microstructural changes in SLM-fabricated AlSi10Mg alloys caused by heat treatment at various temperatures are not yet fully understood.

In the present study, to better understand the microstructure development of SLM-fabricated AlSi10Mg alloy during heat treatment at elevated temperatures, the microstructure and texture of SLM-fabricated AlSi10Mg alloy, heat-treated at different temperatures, was examined and compared with the constitute phases determined by thermodynamic equilibrium calculations. The mechanical properties of the heat-treated SLM AlSi10Mg specimens were examined by conducting tensile tests. The results were then utilized to discuss two issues: (1) the microstructure development process of the SLM AlSi10Mg alloy during heat treatment at elevated temperatures, (2) the effects of the microstructural characteristics on the tensile properties of the SLM AlSi10Mg alloy heat-treated at elevated temperatures.

2. Experimental procedure

In the present study, AlSi10Mg alloy powder [17] with a particle size ranging from 1 μm to 34 μm was used. SEM images of the powder are shown in **Fig. 1(a)**. Details of the selective laser melting (SLM) process used to produce the AlSi10Mg alloy samples are described in the literature [9,10,18]. The nominal compositions of the alloy powder and measured compositions (as analyzed by inductively coupled plasma-atomic emission spectrometry (ICP-AES)) are listed

in **Table 1**. Note that the proportions of the major alloy elements (Si, Mg, and Fe) in the initial powder are almost the same as those in the bulk sample fabricated using SLM. The SLM processing for fabricating the cube samples (45 mm in length) was carried out at room temperature using an EOSINT M 280 additive-manufacturing system, equipped with an Yb laser operating at 380 W (EOS GmbH, Germany). The parameters applied to the fabrication of the samples were as follows; the thickness of the bedded-powder layers was 30 μm , the hatch spacing between the adjacent laser-scanning tracks was approximately 100 μm , and the angle of rotation between the bedded-powder layers was 67°. The laser-scanning track applied in this study is shown schematically in **Fig. 1(b)**. Hereafter, the directions normal and parallel to the bedded-powder layer are designated the Z direction and X/Y direction, respectively. High-purity Ar gas was used in the SLM processing to prevent oxidation of the fabricated sample. The as-fabricated bulk sample was held at 300 °C for 2 h (annealing) or at 530 °C for 6 h (solution-treatment), followed by quenching in water. To enable a comparison with the SLM sample, the studied powder was melted by high-frequency induction and then solidified to prepare an as-cast ingot of the studied AlSi10Mg alloy. Note that the cooling rate in solidification (experimentally measured by K-type thermocouples) is approximately 0.3 °C/s.

Various methods were used to prepare the samples used for the observations. The bulk samples to be observed by optical microscopy were both mechanically and electro-polished with a solution of perchloric acid and ethyl alcohol, at a volume ratio of 1:9 at room temperature. Cross-sectional samples (observed from the X/Y direction) were ion-polished by a cross-section polisher at 5 V. The microstructures were observed by using a scanning electron microscope (SEM) operating at 30 kV. An orientation analysis was carried out by electron backscatter diffraction (EBSD) using step sizes of 0.1 μm and 2 μm . The hardness (HV) of these samples was measured using a Vickers indenter at a constant load of 9.8 N at room temperature. Tensile tests using plate specimens with a gauge length of 14 mm and a thickness of 2 mm were carried out at a strain rate of $1.2 \times 10^{-3}/\text{s}$

(corresponding to a cross-head speed of 1 mm/min) at room temperature. In the present study, tensile test specimens along the X/Y direction were cut out from the center part of the fabricated cube samples. The gage portion of the prepared tensile test specimens along the Z direction was located around the center of the fabricated cube samples. SEM was used to observe the fracture surfaces of the tested specimens.

3. Thermodynamic assessment of AlSi10Mg alloy

A thermodynamic equilibrium calculation for the Al–Si–Mg–Fe quaternary system was carried out using a CALPHAD approach [19–21], based on a thermodynamic database for an Al-based multi-component system (PanAl) [22] for the measured alloy composition of Al–10.8Si–0.2Mg–0.4Fe (wt.%). **Figure 2** presents (a) the composition of the studied AlSi10Mg alloy on a vertical section of the Al–xSi–0.2Mg–0.4Fe (wt.%) of the Al–Si–Mg–Fe quaternary system and (b) the calculated mol fractions of the constituent phases in equilibrium at various temperatures. The calculated phase diagram (**Fig. 2(a)**) indicates the possible solidification path. The liquidus is located at approximately 600 °C and the initial solid phase is α -Al (fcc) for the studied alloy composition. A three-phase region of α -Al + Si(diamond) + β -AlFeSi (τ_6 -Al₉Fe₂Si₂) [23,24] is below the solidus temperature of approximately 540 °C. A four-phase region of α -Al + Si (diamond) + β -AlFeSi + Mg₂Si appears at temperatures lower than 400 °C, whereas the fraction of the Mg₂Si phase in equilibrium is less than 0.3% for the studied alloy composition (**Fig. 2(b)**). **Figure 3** is an optical micrograph showing the microstructure of the as-cast AlSi10Mg ingot, which provides an indication of the solidification path. The dendritic α -Al phase (bright contrast) is the initial solid that is followed by the formation of the fine Si (intermediate contrast) and Fe-containing phases (dark contrast). The observed solidification sequence is in good agreement with the thermodynamic assessment. The detailed result of calculated Scheil solidification sequence for the studied AlSi10Mg alloy is described elsewhere [25]. Note that the calculated phase diagram indicates that the

solution-treatment temperature (530 °C) and annealing temperature (300 °C) correspond to a three-phase region of α -Al + Si (diamond) + β -AlFeSi and a four-phase region of α -Al + Si (diamond) + β -AlFeSi + Mg₂Si, respectively.

4. Results

4.1 Microstructure

Figure 4 presents low-magnification (a, c, e) and high-magnification (b, d, f) images showing the microstructure of the as-fabricated sample (a, b), the sample annealed at 300 °C (c, d), and the sample that was solution treated at 530 °C (e, f). These images were observed from the X/Y direction. The as-fabricated sample (**Fig. 4(a)**) exhibits the characteristic microstructure consisting of melt pools with a half-cylindrical shape (corresponding to the locally melted and rapidly solidified regions) as reported in the literature [10,26,27]. The melt pool height was determined to be approximately 150 μ m while its width was determined to be approximately 300 μ m. The applied hatch spacing of 100 μ m and the powder layer thickness of 30 μ m cause an overlap of a large part of the melt pools between neighboring scan tracks. The melt pools are composed of columnar α -Al grains with a mean width of about 500 nm surrounded by numerous fine Si particles with a mean size of less than 100 nm (**Fig. 4(b)**). These columnar α -Al grains tend to be elongated along the Z direction. The fine Si particles correspond to the α -Al/Si eutectic microstructure in the rapidly solidified regions. After annealing at 300 °C for 2 h, the observed microstructural characteristics changed slightly. The melt pools can be observed (**Fig. 4(c)**), but the Si particles become coarser in some parts (**Fig. 4(d)**). Note that fine Si particles can be observed within the columnar α -Al grains, indicating that the Si (diamond) phase precipitates in the α -Al matrix during annealing. After the solution treatment at 530 °C for 6 h, no melt pools are observed in the optical micrograph (**Fig. 4(e)**). SEM observations (**Fig. 4(f)**) revealed a significant coarsening of the Si particles (**Table 2**) and the formation of an Fe-containing intermetallic phase (β -AlFeSi) with a rod-shaped morphology. The area fraction, density, and mean size of the Si particles, as

quantified by image analysis of the SEM micrographs, are summarized in **Table 2**.

Figure 5 shows the results of an EBSD analysis of the as-fabricated sample (a–c), the sample annealed at 300 °C (d–f), and the sample that was solution treated at 530 °C (g–i). The EBSD analysis revealed that the microstructure of the α -Al matrix consists mostly of elongated grains with a mean width of approximately 10 μm in the as-fabricated sample (**Fig. 5(a)**). In the vicinity of the boundaries between the melt pools, smaller (several μm) equiaxed grains appear. Many of the elongated grains have a $\langle 001 \rangle$ orientation along the Z direction (**Fig. 5(b)**). The $\langle 001 \rangle$ -oriented grains (assuming that the $\langle 001 \rangle$ direction varies from that parallel to the Z direction by no more than 15°) constitute 20% of the area, resulting in the development of a $\{001\}$ texture in the as-fabricated sample (**Fig. 5(c)**). This texture development was found to be in good agreement with the results of a previous study [26]. These microstructural features remain unchanged after annealing at 300 °C (**Fig. 5(d)**). The elongated α -Al grains dominate the microstructure even after the solution treatment at 530 °C for 6 h (**Fig. 5(g)**) as well, whereas the width of the elongated α -Al grains becomes slightly larger. The distribution of the $\langle 001 \rangle$ -oriented grains in the heat-treated samples (**Fig. 5(e, h)**) is almost the same as that in the as-fabricated sample, resulting in the $\{001\}$ texture observed in the heat-treated samples (**Fig. 5(f, i)**). The microstructural parameters of the α -Al matrix are summarized in **Table 2**.

Figure 6 presents the results of the minute EBSD analysis for the elongated α -Al grains in the melt pools of the as-fabricated sample. The elongated α -Al grains radiate from the center of the melt pool, which has a half-cylindrical shape (**Fig. 6(b)**). The center of the melt pool corresponds to the hottest point, resulting from the local heating by laser-beam irradiation, as reported in the literature [27,28]. It is evident that most of the elongated α -Al grains are preferentially oriented in the $\langle 001 \rangle$ direction towards the center of the melt pool (**Fig. 6(c-1)**), which is indicative of the α -Al grains solidifying in the direction of the hottest point of the melt pool, considering the $\langle 001 \rangle$ preferential solidification direction of the α -Al phase [29]. A clear trend is observed in that the α -Al grains with the $[001]$

orientation along the Z direction are elongated along the Z direction (Fig. 5(a, d, g)). Therefore, the development of the {001} texture as observed in the as-fabricated sample is responsible for the solidification of α -Al phase in the $\langle 001 \rangle$ orientation in the locally laser-melted regions.

Figure 7 shows the distribution of the boundary misorientation angles as measured by EBSD analysis. To quantify the average grain size of the as-fabricated sample, the total length of the high-angle boundaries in the EBSD-analyzed area ($1 \text{ mm} \times 1 \text{ mm}$) was measured. Assuming that the measured area is representative of the three-dimensional morphology of the observed characteristic microstructure, the area of the high-angle boundaries per unit volume, S_v , is $0.248 \mu\text{m}^{-1}$. It is generally known, based on quantitative microscopy [30], that there is a simple relationship between S_v and the mean intercept length (L) for a mass of any three-dimensional shape, $S_v = 2/L$. Using this equation, we find that the mean spacing of the high-angle boundaries is $7.6 \mu\text{m}$. This can be regarded as being the mean grain size of the as-fabricated sample. The mean spacing of the high-angle boundaries increases slightly to $8.6 \mu\text{m}$ after the solution treatment at 530°C , which demonstrates that a slight grain growth occurs in the α -Al matrix at elevated temperatures. It can be recognized that, in the as-fabricated sample (Fig. 7(a)), the distribution of the boundary misorientation angle is relatively flat but has two peaks, at $2\text{--}4^\circ$ and at around 45° . The peak located at a misorientation angle of around 2° suggests the presence of high-density, low-angle boundaries within the columnar α -Al grains. The fraction of the high-angle boundaries and the mean misorientation angle are 83% and 33° , respectively. These trends in the misorientation angle distribution can be found in the sample annealed at 300°C (Fig. 7(b)) as well as in the sample that was solution treated at 530°C (Fig. 7(c)), whereas the peak located at a misorientation of around 2° becomes broader after annealing.

To identify the substructure consisting of low-angle boundaries within the elongated α -Al grains in the as-fabricated sample, a detailed EBSD analysis using a smaller step size of $0.1 \mu\text{m}$ was performed. The results are shown in Fig. 8. The

EBSD analysis revealed the presence of a fine substructure consisting of low-angle boundaries within the elongated grains surrounded by high-angle boundaries (Fig. 8(b)). The mean spacing of the low-angle boundaries in the elongated substructure is less than 2 μm . This fine substructure may contribute to a high peak located at around 2° in the boundary misorientation distribution (Fig. 7(a)), since it could be difficult to detect by macroscopic EBSD analysis using a step size of 2 μm (Fig. 5). The low-angle boundaries were predominantly located along the aligned fine Si particles corresponding to the $\alpha\text{-Al/Si}$ eutectic microstructure (Fig. 8(c)), such that there are scarcely any low-angle boundaries within the columnar $\alpha\text{-Al}$ grains in the primary solidified phase.

Figure 9 presents the results of detailed EBSD analysis using a step size of 0.1 μm for the sample solution treated at 530 $^\circ\text{C}$ for 6 h. The SEM image (Fig. 9(a)) corresponds to region (a) in the orientation color map (Fig. 9(b)). Note that the streaking observed in the SEM image (Fig. 9(a)) corresponds to contamination derived from the prior EBSD analysis (electron scanning). The detailed EBSD analyses demonstrate that low-angle boundaries are scarcely observed in the $\alpha\text{-Al}$ grains surrounded by high-angle boundaries (Fig. 9(c, d)), which is distinct from the presence of high-density low-angle boundaries in the as-fabricated sample (Fig. 8). To quantify the density of the low-angle boundaries within the $\alpha\text{-Al}$ grains, the lengths of the boundaries per unit area were plotted as a function of the boundary misorientation, based on the results of EBSD analyses using a step size of 0.1 μm . The results are shown in Fig. 10. The distribution of the boundary misorientation angle shows a high peak at around 6° in the as-fabricated sample (Fig. 10(a)), whereas the peak becomes much lower in the annealed sample (Fig. 10(b)). No peaks are recognized in the solution-treated sample (Fig. 10(c)). These results indicate that the fine substructure consisting of low-angle boundaries is destroyed at elevated temperatures.

4. 2 Mechanical properties

Figure 11 shows the Vickers hardness of the studied samples, together with the

change in hardness of the solution-treated sample (530 °C/6 h) with natural aging (at room temperature). The hardness of the as-fabricated sample significantly decreases from 132 HV to 88 HV after annealing at 300 °C for 2 h. After the solution treatment at 530 °C for 6 h, the hardness decreased to approximately 60 HV. Natural age hardening (at room temperature) was identified in the solution-treated sample. The hardness increases with the natural aging time, reaches 75 HV, and then nearly saturates after 10^3 ks. The natural age hardening is probably caused by the precipitation of the Mg₂Si phase or its associated metastable phases, according to the calculated phase diagram (Fig. 2).

Figure 12 shows the nominal stress–strain curves of specimens that are tensile-deformed in the (a) X/Y direction and (b) Z direction. The tensile properties of the as-fabricated samples vary according to the tensile direction. In the case of tensile deformation along the X/Y direction, the as-fabricated specimen exhibits a yield strength of 280 MPa. The flow stress increases at a relatively high strain hardening rate and then reaches a maximum of approximately 480 MPa. The tensile elongation was around 8%. In its counterpart in the Z direction, the yield strength is approximately 230 MPa, which is lower than that deformed in the X/Y direction, whereas the maximum stress (tensile strength) is at the same level. The tensile elongation was approximately 5%, which is lower than that in the X/Y direction. A similar direction dependency of the tensile properties has been reported [31]. The direction-dependence of the tensile ductility was observed in the specimen annealed at 300 °C. The annealed specimen exhibits a lower strength and higher elongation, which is independent of the tensile direction. In the solution-treated specimen, no direction-dependence of its tensile properties was observed. Note that any deviation in its tensile strength would be associated with age hardening at ambient temperatures (Fig. 11). These results indicate that heat treatment at elevated temperatures could reduce the direction-dependence of the tensile properties of the as-fabricated specimen. The tensile properties of the studied specimens are summarized in **Table 3**.

Macroscopic fractographs of the tensile-tested specimens are shown in **Fig. 13**.

Numerous spherical dimples were found over the entire fracture surface in all the specimens, which is indicative of ductile fracture. It should be noted that, in the as-fabricated specimen and that annealed at 300 °C before being tensile-deformed in the Z direction, several band-shaped surface areas with a width of approximately 200 μm were macroscopically observed (Fig. 13(d, e)), which corresponds to the morphologies of the melt pools observed in the as-fabricated sample (Fig. 4). These fractographs were observed in a previous study [32]. The unique fracture surfaces demonstrate that fracture occurs around the boundaries between the melt pools. Note that these observations also revealed fine dimples on the band-shaped surface areas, indicating the occurrence of ductile rather than brittle fracture.

5. Discussion

5.1 Change in Microstructure with Heat Treatment

The present study set out to investigate the microstructures and crystallographic features of SLM AlSi10Mg alloys that had been heat-treated at different temperatures, to determine the coarsening of the fine Si particles surrounding the columnar α -Al phase during heat treatment at elevated temperatures (Fig. 4). One of the important findings was the observation of finely distributed Si particles within the columnar α -Al phase after annealing at 300 °C (Fig. 4). The observed fine Si precipitates in the columnar α -Al phase indicate the existence of Si supersaturation in the columnar α -Al matrix of the as-fabricated sample. To identify whether the α -Al matrix contains solute Si in supersaturation, the area fraction of the Si particles was quantified by image analysis of SEM micrographs (Table 2). Figure 14 presents the measured fractions of Si particles in the studied samples, together with the calculated volume fraction of the Si phase in equilibrium, as determined by thermodynamic assessment. The average measured fraction in the as-fabricated sample was 10.3%, which is lower than the calculated volume fraction of the Si phase in equilibrium (11.8%). This comparison demonstrates the presence of a certain amount of Si in solution in the columnar

α -Al phase of the as-fabricated sample, which is supported by the observation of fine Si precipitates within the columnar α -Al grains of the annealed sample (Fig. 4(d)). It is noteworthy that the difference between the measured and calculated values becomes smaller with an increase in the temperature used for the heat treatment. The measured fraction of Si particles in the solution-treated sample was almost the same as that of the calculated equilibrium sample at 530 °C, indicating that a microstructural equilibrium is almost reached after the sample is held at that temperature for 6 h. This is in reasonably good agreement with the thermodynamically stable phase of β -AlFeSi (Fig. 2) observed in the solution-treated sample (Fig. 4(f)).

The EBSD analysis performed as part of the present study revealed a slight change in the microstructure of the α -Al matrix during the heat treatment (Fig. 5). The mean spacing of the high-angle boundaries (equivalent to a mean grain size) was found to increase slightly with the heat treatment temperature, whereas the [001] texture was observed in all the studied samples (Table 2). It is intriguing that a fine substructure consisting of low-angle boundaries is present within the elongated α -Al grains in the as-fabricated sample (Fig. 8). This substructure was barely observable in the sample heat-treated at 530°C (Figs. 9, 10). Together, these facts suggest that a microstructural change is likely due to the recovery process (annihilation of the dislocations [33]) at elevated temperatures, when considering a low-angle boundary made up of a tangled array of dislocations. Note that these finely distributed Si particles could play a significant role in the pinning of the grain boundary migration in the α -Al matrix, resulting in the inhibition of the coarsening of the microstructure due to recrystallization or grain growth [33].

Based on the aforementioned discussion, the development process of the microstructure in SLM AlSi10Mg alloy at elevated temperatures can be schematically illustrated, as shown in Fig. 15. In the as-fabricated sample, the fine columnar α -Al grains (initially solid) surrounded by fine eutectic Si particles (corresponding to the Si-rich liquid with a lower melting temperature) in the melt pools developed through local melting and rapid solidification by the SLM process

(Fig. 15(a)). The columnar α -Al grains feature a fine substructure consisting of a tangled array of dislocations. At elevated temperatures (Fig. 15(b)), the fine Si phase precipitates within the columnar α -Al phase and the eutectic Si particles become coarser. Within the α -Al matrix, the developed substructure disappears, presumably due to the elimination of dislocations through the recovery process at elevated temperatures. At higher temperatures (Fig. 15(c)), not only further coarsening of the Si phase but also the formation of a stable intermetallic phase occurs, such that microstructural equilibrium is reached after long-term exposure. This distributed Si phase could inhibit the grain boundary migration, which maintains the fine microstructure of the α -Al matrix developed by the SLM process, even at high temperatures. Note that the α -Al phase includes a certain amount of Mg and Si in solution at 530 °C, resulting in age-hardening at lower temperatures (Fig. 11) due to the formation of the Mg_2Si phase or its associated metastable phases.

5.2 Mechanical Properties Associated with Microstructure

In the present study, the mechanical properties of AlSi10Mg alloys that were selectively laser-melted and subsequently heat-treated at different temperatures were subjected to tensile tests. The tensile tests demonstrated the direction dependence of the tensile ductility of the as-fabricated specimen (Fig. 12, Table 3). Fractographs of the specimens that were tensile-tested in the Z direction showed that a fracture occurred in the vicinity of the boundaries between the melt pools (Fig. 13(d)). The fracture mode was responsible for the observed direction-dependence of the tensile ductility. An important finding of the present study is that the specimen annealed at 300 °C showed similar trends in its tensile ductility (Fig. 12, Table 3) and fracture surfaces (Fig. 13(e)) as the as-fabricated specimen. Considering the observation of a slight change in the microstructure of the α -Al matrix as a result of the heat treatments (Fig. 4), we can say that the Si particles that are finely distributed at the equiaxed α -Al grains around the boundaries between the melt pools are the dominant contributor to the initiation of

a fracture. The fine Si particles would enhance the local strain-hardening in the α -Al matrix, resulting in crack initiation within the α -Al grains located at the boundaries between the melt pools. This fact suggests that changing the distribution of the Si particles would be an effective means of controlling the direction-dependence of the tensile ductility of AlSi10Mg alloy fabricated by SLM.

It is particularly interesting that annealing at 300°C significantly reduced the strength of the as-fabricated specimen from 470 MPa to 280 MPa (Table 3), regardless of the slight differences in the microstructure as detected by SEM and EBSD analyses (Fig. 4). One possible reason for the reduced strength is the destruction of the fine substructures developed within the α -Al elongated grains (Fig. 8, Fig. 9). The substructure consisted of a tangled array of dislocations, and is thus able to sustain a higher internal stress within the α -Al grains. Another possible contributor to the lower strength is the reduced solid solution hardening due to the precipitation of the fine Si phase during the annealing (Fig. 14). However, there is still the issue of identifying the dominant contributor to the high strength of the AlSi10Mg alloy fabricated by SLM. To clarify the strengthening mechanism, high-resolution transmission electron microscopy (TEM) observations will be necessary. In a recent study [34], TEM observations indicated that the sub-boundaries and Si particles within the columnar grains might limit the dislocation movement during deformation in an AlSi10Mg alloy fabricated by SLM. Thus, it will be necessary to perform further TEM observations of the dislocation substructure and the nano-sized Si particles within the observed columnar α -Al grains, as well as their changes at elevated temperatures, to better understand the strength of Al alloys fabricated by additive manufacturing.

5. Summary

The present study investigated how heat treatment changed the microstructure and mechanical properties of an AlSi10Mg alloy that had been fabricated using selective laser melting (SLM). The results of the investigation were then utilized

in conjunction with thermodynamic assessments to understand the microstructure development of an AlSi10Mg alloy fabricated by SLM, as well as its related mechanical properties. The following conclusions can be drawn:

(1) The as-fabricated AlSi10Mg alloy exhibits a characteristic microstructure consisting of melt pools with a half-cylindrical shape (corresponding to locally melted and rapidly solidified regions). The melt pools consisted of a number of columnar α -Al grains surrounded by fine eutectic Si particles. A fine dislocation substructure consisting of low-angle boundaries is present within the columnar α -Al grains. The observed {001} texture along the Z direction could be attributed to the preferential $\langle 001 \rangle$ growth direction of the α -Al phase during the solidification.

(2) In the AlSi10Mg alloy that was held at an elevated temperature, the Si phase was found to finely precipitate within the columnar α -Al phase such that coarsening of the eutectic Si particles occurs. These fine Si particles would inhibit the migration of the grain boundary, thus maintaining the characteristic microstructure and texture of the α -Al matrix as developed by the SLM process. In addition, the destruction of the dislocation substructure occurs in the α -Al matrix as a result of the recovery process. At higher temperatures, not only does further coarsening of Si phase occur, but a stable intermetallic phase forms, reaching microstructural equilibrium after the long-term exposure.

(3) The as-fabricated AlSi10Mg alloy exhibits a high strength of approximately 480 MPa that is independent of the specimen geometry associated with the fabrication direction. In contrast, the tensile ductility is found to be direction-dependent, and is thus responsible for the fracture preferentially occurring at the melt pool boundaries. This direction dependence of the tensile ductility was not observed in the solution-treated specimen with coarsened Si particles. The present result provides an important insight into the control of the direction dependence of the tensile ductility of AlSi10Mg alloy fabricated by SLM.

Acknowledgement

The support of the “Knowledge Hub Aichi”, a Priority Research Project of Aichi Prefectural Government, Japan is gratefully acknowledged. We are grateful for the expert guidance on thermodynamic assessment provided by Mr. K. Hashimoto of Materials Design Technology Co., Ltd., and that on sample preparation provided by Mr. H. Tauchi of WhiteImpact Co., Ltd.

REFERENCES

- [1] M. F. Ashby, A. Evans, N. A. Fleck, J. W. Hutchinson, H.N.G. Wadley, *Metals Foams: A Design Guide*, Elsevier Science (2000).
- [2] J. Banhart, *Manufacture, characterisation and application of cellular metals and metal foams*, *Prog. Mater. Sci.* 46 (2001) 559–632.
- [3] L. P. Lefebvre, J. Banhart and D. Dunand, *Porous Metals and Metallic Foams: Current Status and Recent Developments*, *Adv. Eng. Mater.* 10 (2008) 775-786.
- [4] J. Banhart, *Light-Metal Foams--- History of Innovation and Technological Challenges*, *Adv. Eng. Mater.* 15 (2013) 82-111.
- [5] F. García-Moreno, *Commercial Applications of Metal Foams: Their Properties and Production*, *Materials* 9 (2016), 85.
- [6] E. Koza, M. Leonowicz, S. Wojciechowski, F. Simancik, *Compressive strength of aluminium foams*, *Mater. Let.* 58 (2003) 132-135.
- [7] N. Kanetake, M. Kobashi, *Porous Aluminum*, *Journal of The Japan Institute of Light Metals (in Japanese)*, 62 (2012) 122-134.
- [8] W. E. King, A. T. Anderson, R. M. Ferencz, N. E. Hodge, C. Kamath, S. A. Khairallah, A. M. Rubenchi, *Laser powder bed fusion additive manufacturing of metals; physics, computational, and materials challenges*, *App. Phys. Rev.* 2 (2015) 041304.
- [9] W. J. Sames, F. A. List, S. Pannala, R. R. Dehoff, S. S. Babu, *The metallurgy and processing science of metal additive manufacturing*, *International Materials Reviews* 61 (2016) 1-46.
- [10] D. Herzog, V. Seyda, E. Wycisk, C. Emmelmann, *Additive manufacturing of metals*, *Acta Mater.* 117 (2016) 371-392.
- [11] C. Beyer, D. Figueroa, *Design and Analysis of Lattice Structures for Additive Manufacturing*, *ASME J. Manuf. Sci. Eng.* 138 (2016), 121014-1-15.
- [12] C. Qiu, S. Yue, N. J. E. Adkins, M. Ward, H. Hassanin, P. D. Lee, P. J. Withers, M. M. Attallah, *Influence of processing conditions on strut structure and compressive properties of cellular lattice structures fabricated by selective laser melting*, *Mater. Sci.*

- Eng. A 628 (2015) 188-197.
- [13] I. Maskery, N. T. Aboulkhair, A. O. Aremu, C. J. Tuck, I. A. Ashcroft, R. D. Wildman, R. J. M. Hague, A mechanical property evaluation of graded density Al-Si10-Mg lattice structures manufactured by selective laser melting, *Mater. Sci. Eng. A* 670 (2016) 264-274.
- [14] T. Kimura, T. Nakamoto, Microstructure and Mechanical Properties of Al-10%Si-0.4%Mg Fabricated by Selective Laser Melting, *J. Jpn. Soc. Powder Powder Metallurgy* 61 (2014), 531-537.
- [15] N. T. Aboulkhair, I. Maskery, C. Tuck, I. Ashcroft, N. M. Everitt, The microstructure and mechanical properties of selectively laser melted AlSi10Mg: The effect of a conventional T6-like heat treatment, *Mater. Sci. Eng. A* 667 (2016) 139-146.
- [16] J. Fiocchi, A. Tuissi, P. Bassani, C. A. Biffi, Low temperature annealing dedicated to AlSi10Mg selective laser melting products, *J. Alloys Compd.* 695 (2017) 3402-3409.
- [17] EOS GmbH - Electro Optical Systems, Material data sheet EOS Aluminum AlSi10Mg: https://www.eos.info/m-solutions/material_parameter/download/Aluminium_AlSi10Mg.pdf, 2014 (accessed 17.05.01).
- [18] N. Read, W. Wang, K. Essa, M. M. Attallah, Selective laser melting of AlSi10Mg alloy: process optimisation and mechanical properties development, *Mater. Des.* 65 (2015) 417-424.
- [19] Y. A. Chang, S. Chen, F. Zhang, X. Yan, F. Xie, R. Schmid-Fetzer, W. A. Oates, Phase diagram calculation: past, present and future, *Prog. Mater. Sci.* 49 (2004) 313-345.
- [20] Y. Du, Y. A. Chang, S. Liu, B. Huang, F. Y. Xie, Y. Yang, S. L. Chen, Thermodynamic Description of the Al-Fe-Mg-Mn-Si System and Investigation of Microstructure and Microsegregation During Directional Solidification of an Al-Fe-Mg-Mn-Si Alloy, *Z. Metallkd.* 96(2005), 1351-1362.
- [21] CompuTherm LLC, CompuTherm Database User's Guide, pp. 1-11, http://www.compuTherm.com/download/Database2016_Manual.pdf, 2016 (accessed 17.05.01).
- [22] X. Y. Yan, Y. A. Chang, F. Y. Xie, S. L. Chen, F. Zhang, S. Daniel, Calculated phase diagrams of aluminum alloys from binary Al-Cu to multicomponent commercial alloys, *J. Alloys Compd.* 320 (2001) 151-160.
- [23] C. Rømming, V. Hansen, J. Gjonnes, Crystal structure of β -Al_{4.5}FeSi, *Acta Cryst.* 40 (1994) 307-312.
- [24] M. C. J. Marker, B. Skolyszewska-Kühberger, H. S. Effenberger, C. Schmetterer, K. W. Richter, Phase equilibria and structural investigations in the system Al-Fe-Si, *Intermetallics* 19 (2011) 1919-1929.
- [25] N. Takata, H. Kodaira, K. Sekizawa, A. Suzuki, M. Kobashi, Microstructure and Mechanical Properties of Al-10Si-0.4Mg Alloy Fabricated by Selective Laser Melting,

- Journal of The Japan Institute of Light Metals (in Japanese), 67 (2017) in press.
- [26] L. Thijs, K. Kempen, J. P. Kruth, J. V. Humbeeck, Fine-structured aluminium products with controllable texture by selective laser melting of pre-alloyed AlSi10Mg powder, *Acta Mater.* 61(2013) 1809-1819.
- [27] T. G. Holesinger, J. S. Carpenter, T. J. Lientert, B. M. Patterson, P. A. Papin, H. Swenson, N. L. Cordes, Characterization of an Aluminum Alloy Hemispherical Shell Fabricated via Direct Metal Laser Melting, *JOM* 68 (2016) 1000-1011.
- [28] X. Ding, L. Wang, Heat transfer and fluid flow of molten pool during selective laser melting of AlSi10Mg powder: Simulation and experiment, *J. Manuf. Proc.* 26 (2017) 280-289.
- [29] W. Kurz, D.J. Fisher, *Fundamentals of Solidification*, third ed., Trans Tech, Switzerland, 1989.
- [30] R. T. DeHoff, F. N. Rhines (eds.), *Quantitative Microscopy*. New York: McGraw-Hill 1968.
- [31] L. Hitzler, C. Janousch, J. Schanz, M. Merkel, B. Heine, F. Mack, W. Hall, A. Öchsner, Direction and location dependency of selective laser melted AlSi10Mg specimens, *J. Mater. Proc. Tech.* 243 (2017) 48-61.
- [32] I. Rosenthal, A. Stern, N. Frage, Strain rate sensitivity and fracture mechanism of AlSi10Mg parts produced by Selective Laser Melting, *Mater. Sci. Eng. A* 682 (2017) 509-517.
- [33] F. J. Humphreys, M. Hatherly, *Recrystallization and Related Annealing Phenomena*, Second Edition, Elsevier, 2004.
- [34] J. Wu, X. Q. Wang, W. Wang, M. M. Attallah, M. H. Loretto, Microstructure and strength of selectively laser melted AlSi10Mg, *Acta mater.* 117 (2016) 311-320.

Captions

Table 1 Chemical composition of studied AlSi10Mg alloy (wt%)

Table 2 Microstructural parameters of AlSi10Mg alloy specimens fabricated by selective laser melting and subsequently heat-treated at different temperatures

Table 3 Tensile properties of AlSi10Mg alloy specimens fabricated by selective laser melting and subsequently heat-treated at different temperatures

Figure 1 (a) SEM images of initial AlSi10Mg alloy powder used in this study and (b) schematic showing laser scanning tracks with 67° rotation on each powder layer.

Figure 2 (a) Vertical section of Al-0.2Mg-0.4Fe (wt%) in Al-Si-Mg-Fe quaternary phase diagram and (b) mol fractions of constitute phases in Al-10.8Si-0.2Mg-0.4Fe alloy in equilibrium.

Figure 3 Optical micrograph of microstructure of as-cast AlSi10Mg alloy (ingot prepared by melting alloy powder).

Figure 4 (a, c, e) Optical micrographs and (b, d, f) SEM images showing microstructures of the AlSi10Mg alloy samples: (a, b) as-fabricated, (c, d) annealed at 300°C for 2 h, (e, f) heat-treated at 530°C for 6 h.

Figure 5 (a,d,g) Orientation color maps, (b,d,f) distribution maps of [001] oriented regions (Less than a 15° deviation was tolerated from the [001] direction parallel to the Z direction) and (c,f,i) 001 pole figures of the AlSi10Mg alloy samples: (a,b) as-fabricated, (c,d) annealed at 300°C for 2 h, (e,f) heat-treated at 530°C for 6 h.

Figure 6 (a) Orientation color map, (b) selected-area (melt pool) color map and (c–g) corresponding 001 pole figures and (h–l) schematic cubic unit cell representing the orientation of elongated grains in the as-fabricated AlSi10Mg alloy.

Figure 7 (a) Misorientation angle distribution in (a) as-fabricated sample, (b) $300^\circ\text{C}/2$ h annealed sample, $530^\circ\text{C}/6$ h heat-treated sample, as obtained by EBSD analysis at a scanning step size of $2.0\ \mu\text{m}$.

Figure 8 (a) SEM image and (b, c) corresponding orientation color maps (obtained by EBSD

analysis) showing the microstructure of the as-fabricated AlSi10Mg alloy. In Fig. 8(b), the fine lines represent the misorientation (θ) of $1 < \theta < 15^\circ$, while the bold lines represent $\theta > 15^\circ$. The green regions in (c) represent the locations of the Si particles.

Figure 9 (a) SEM image and (b–d) corresponding orientation color maps (obtained by EBSD analysis) showing the microstructure of the AlSi10Mg alloy solution treated at 530°C for 6 h. In Fig. 9(b–d), the fine lines represent the misorientation (θ) of $1 < \theta < 15^\circ$, while the bold lines represent $\theta > 15^\circ$.

Figure 10 Length of boundaries per unit area as a function of misorientation angle in (a) as-fabricated sample, (b) $300^\circ\text{C}/2$ h annealed sample, $530^\circ\text{C}/6$ h heat-treated sample, which were obtained by EBSD analysis with a scanning step size of $0.1\ \mu\text{m}$.

Figure 11 Change in hardness of solution-treated AlSi10Mg alloy ($530^\circ\text{C}/6$ h) with aging time at room temperature, together with hardness of as-fabricated sample and subsequently annealed sample.

Figure 12 Nominal stress-strain curves of AlSi10Mg specimens measured by tensile tests at room temperature: (a) tensile direction normal to Z direction, (b) tensile direction parallel to Z direction.

Figure 13 Fracture surfaces of (a, d) as-fabricated specimen, (b, e) annealed specimen ($300^\circ\text{C}/2$ h) and (c, f) solution-treated specimen ($530^\circ\text{C}/6$ h): (a–c) tensile direction normal to Z direction, (d–f) tensile direction parallel to Z direction.

Figure 14 Experimentally measured area fractions of Si particles in studied samples as a function of heat treatment temperature, together with calculated volume fraction of studied composition in equilibrium.

Figure 15 Schematic showing change in microstructure of selectively laser-melted AlSi10Mg alloy, as a result of heat treatment.

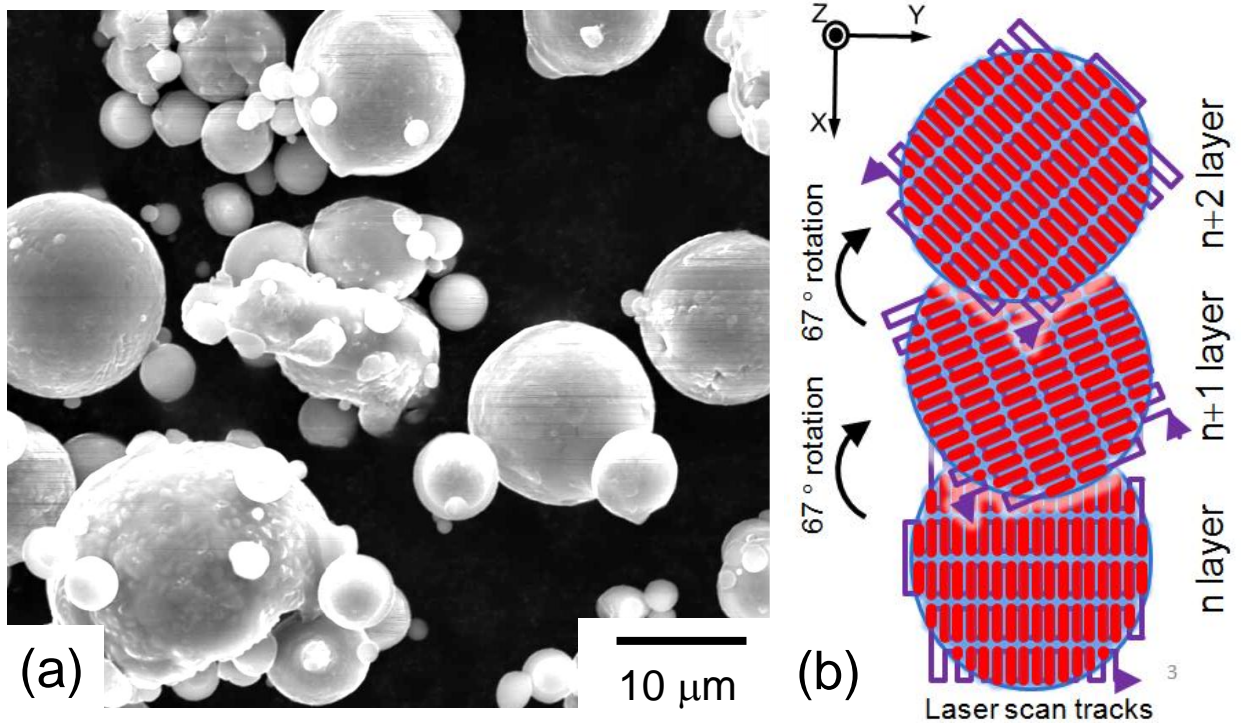


Figure 1 (a) SEM images of initial AlSi10Mg alloy powder used in this study and (b) schematic showing laser scanning tracks with 67° rotation on each powder layer.

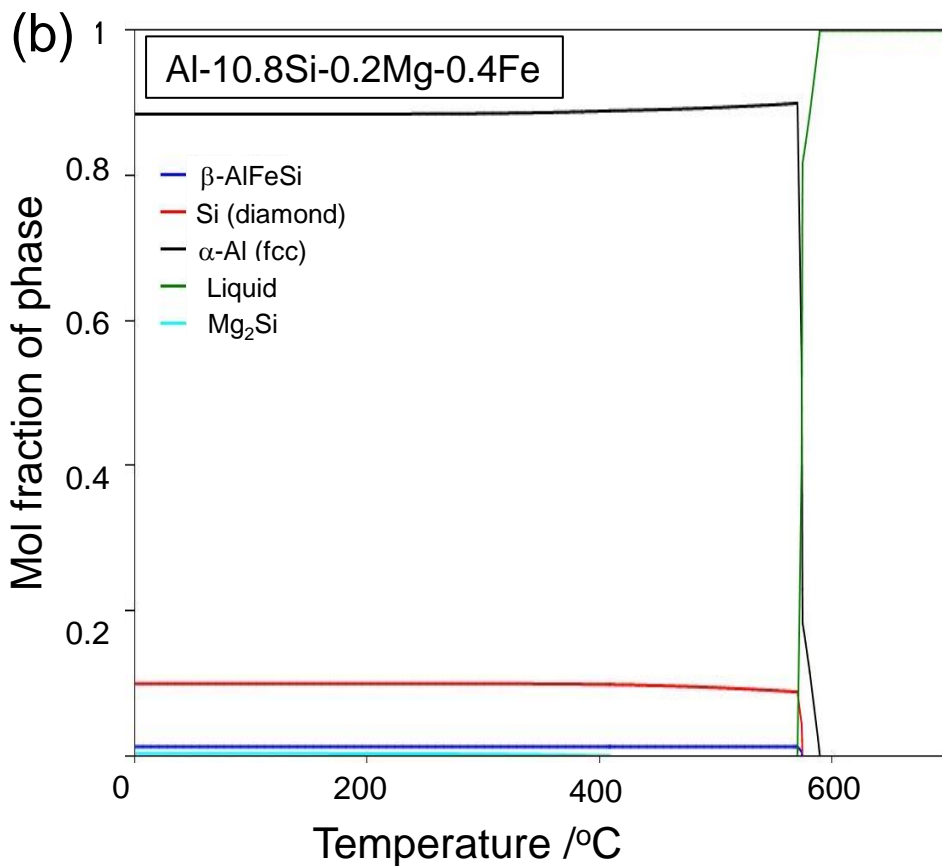
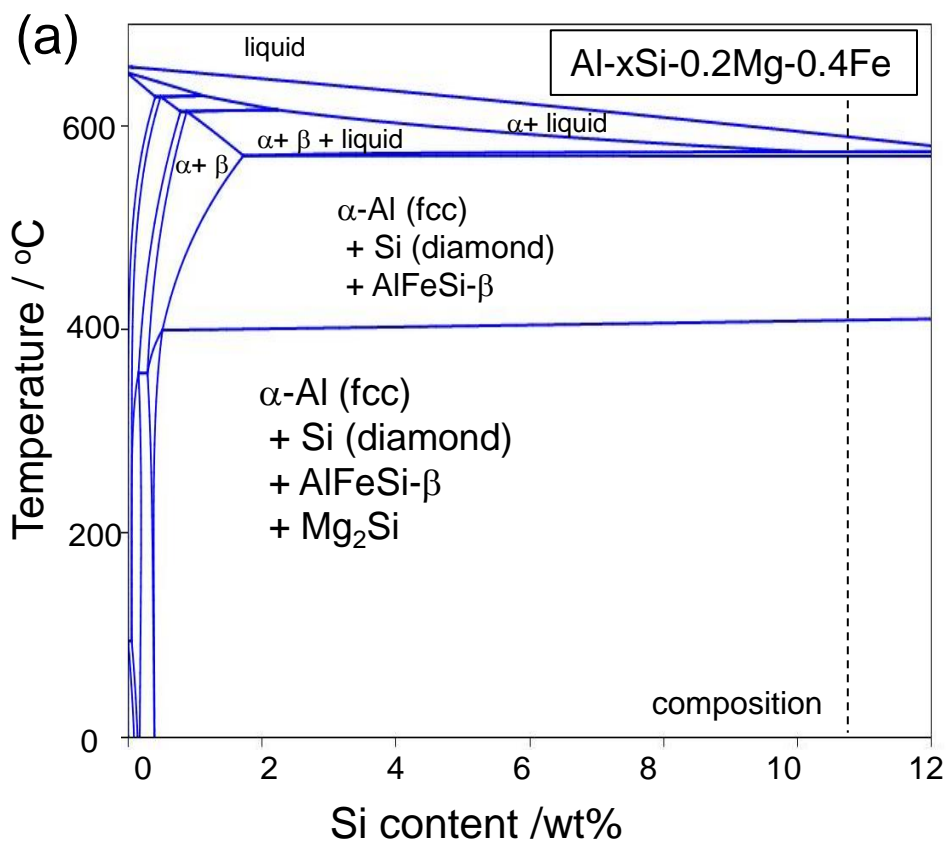


Figure 2 (a) Vertical section of Al-0.2Mg-0.4Fe (wt%) in Al-Si-Mg-Fe quaternary phase diagram and (b) mol fractions of constitute phases in Al-10.8Si-0.2Mg-0.4Fe alloy in equilibrium.

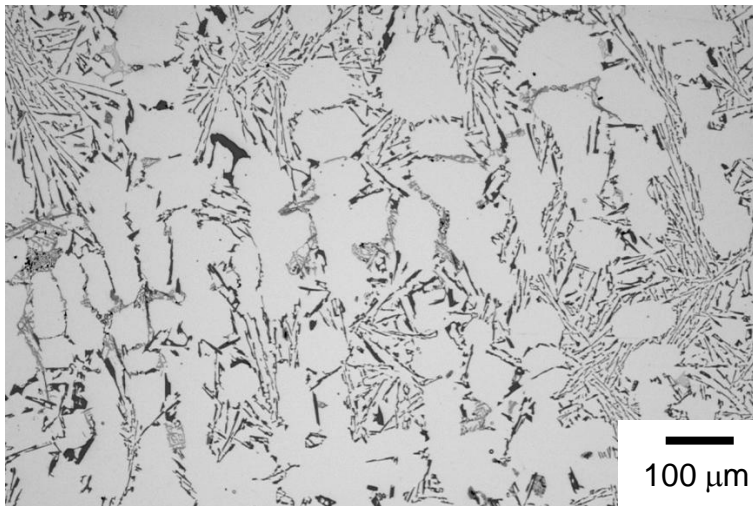


Figure 3 Optical micrograph of microstructure of as-cast AlSi10Mg alloy (ingot prepared by melting alloy powder).

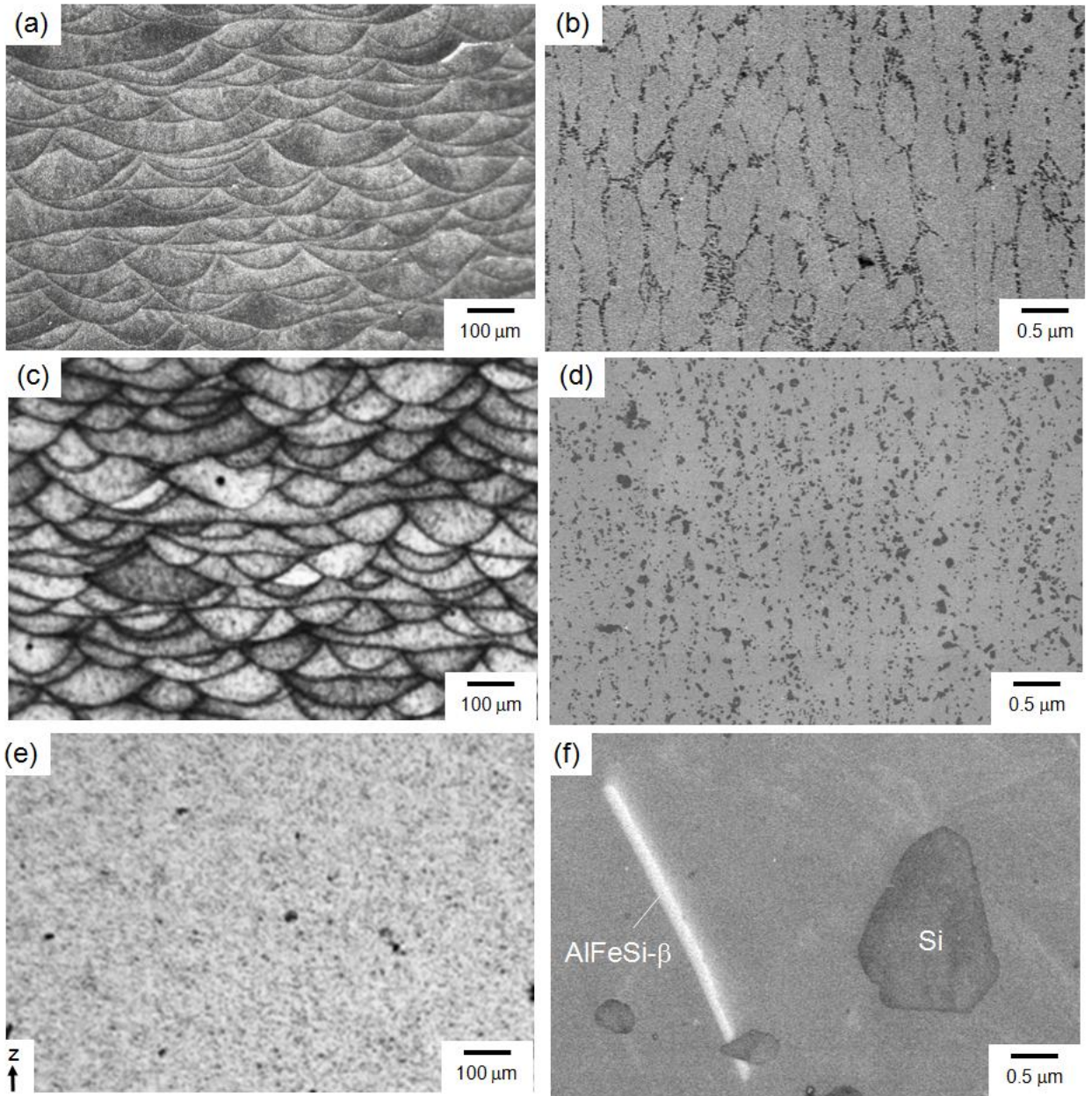


Figure 4 (a, c, e) Optical micrographs and (b, d, f) SEM images showing microstructures of the AlSi10Mg alloy samples: (a, b) as-fabricated, (c, d) annealed at 300° C for 2 h, (e, f) heat-treated at 530° C for 6 h.

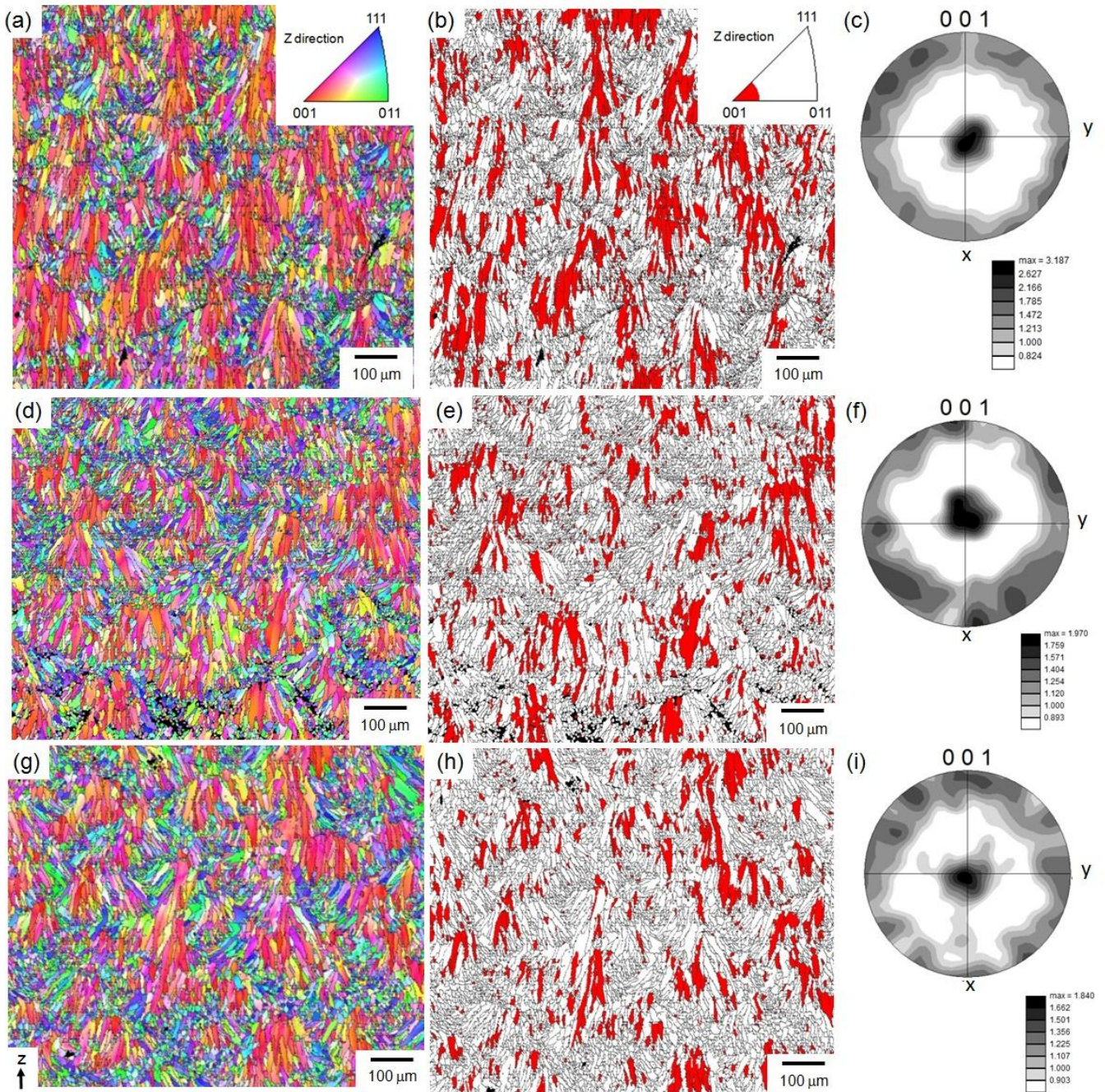


Figure 5 (a,d,g) Orientation color maps ,(b,d,f) distribution maps of [001] oriented regions (Less than a 15° deviation was tolerated from the [001] direction parallel to the Z direction) and (c,f,i) 001 pole figures of the AlSi10Mg alloy samples: (a,b) as-fabricated, (c,d) annealed at 300°C for 2 h, (e,f) heat-treated at 530°C for 6 h.

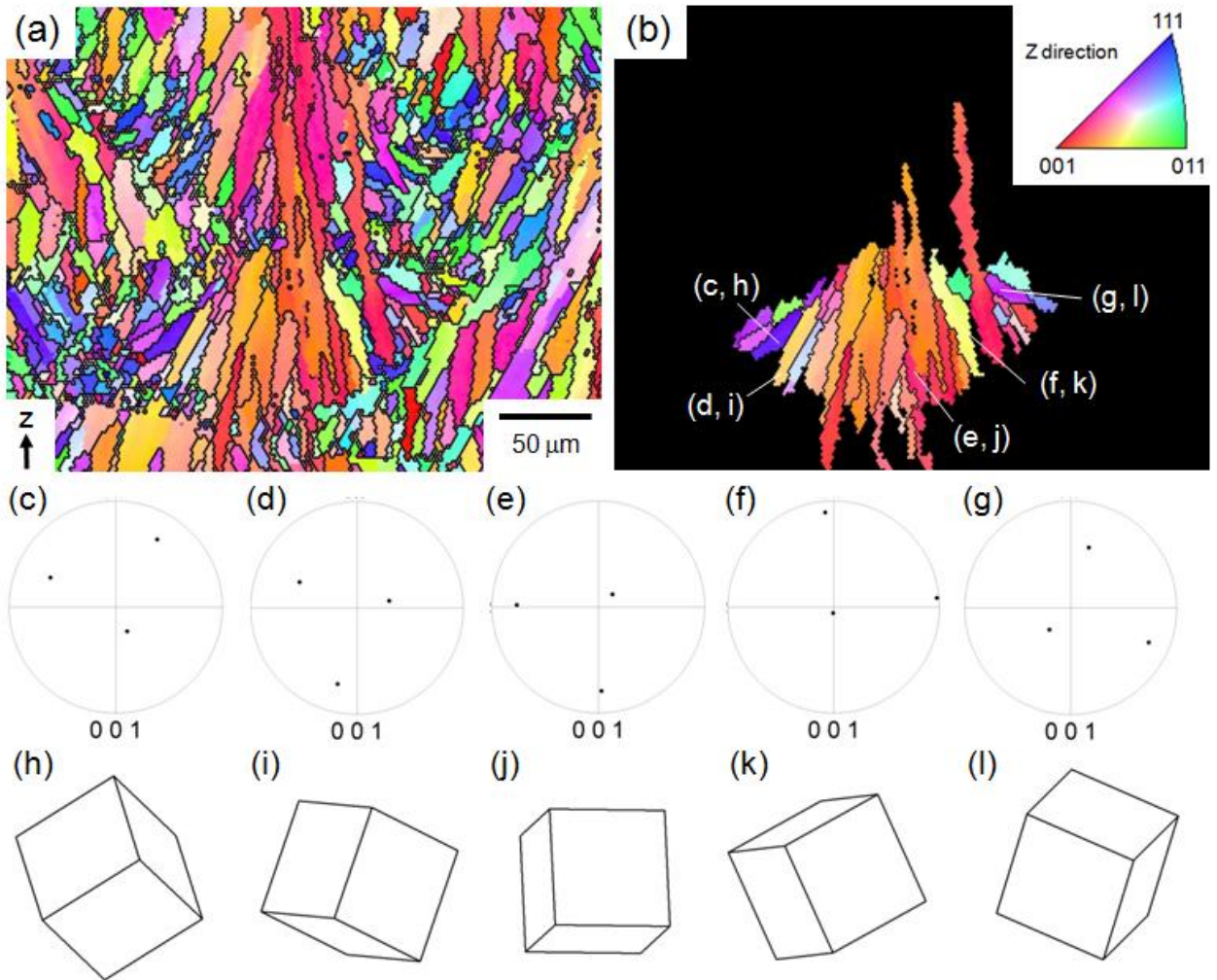


Figure 6 (a) Orientation color map, (b) selected-area (melt pool) color map and (c–g) corresponding 001 pole figures and (h–l) schematic cubic unit cell representing the orientation of elongated grains in the as-fabricated AlSi10Mg alloy.

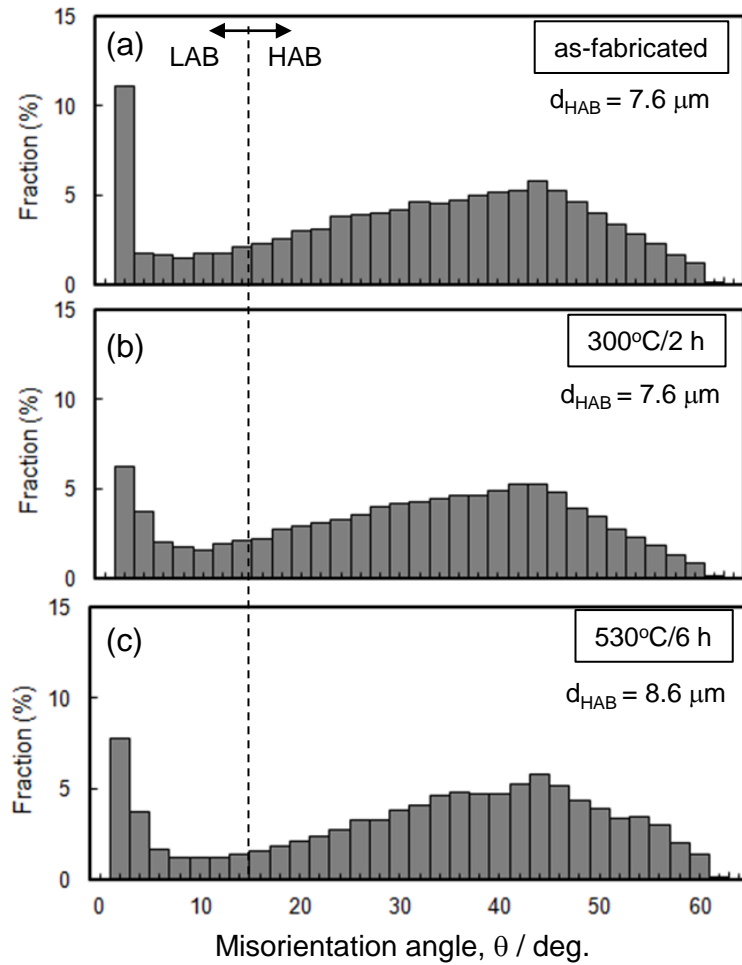


Figure 7 (a) Misorientation angle distribution in (a) as-fabricated sample, (b) $300^\circ\text{C}/2 \text{ h}$ annealed sample, $530^\circ\text{C}/6 \text{ h}$ heat-treated sample, as obtained by EBSD analysis at a scanning step size of $2.0 \mu\text{m}$.

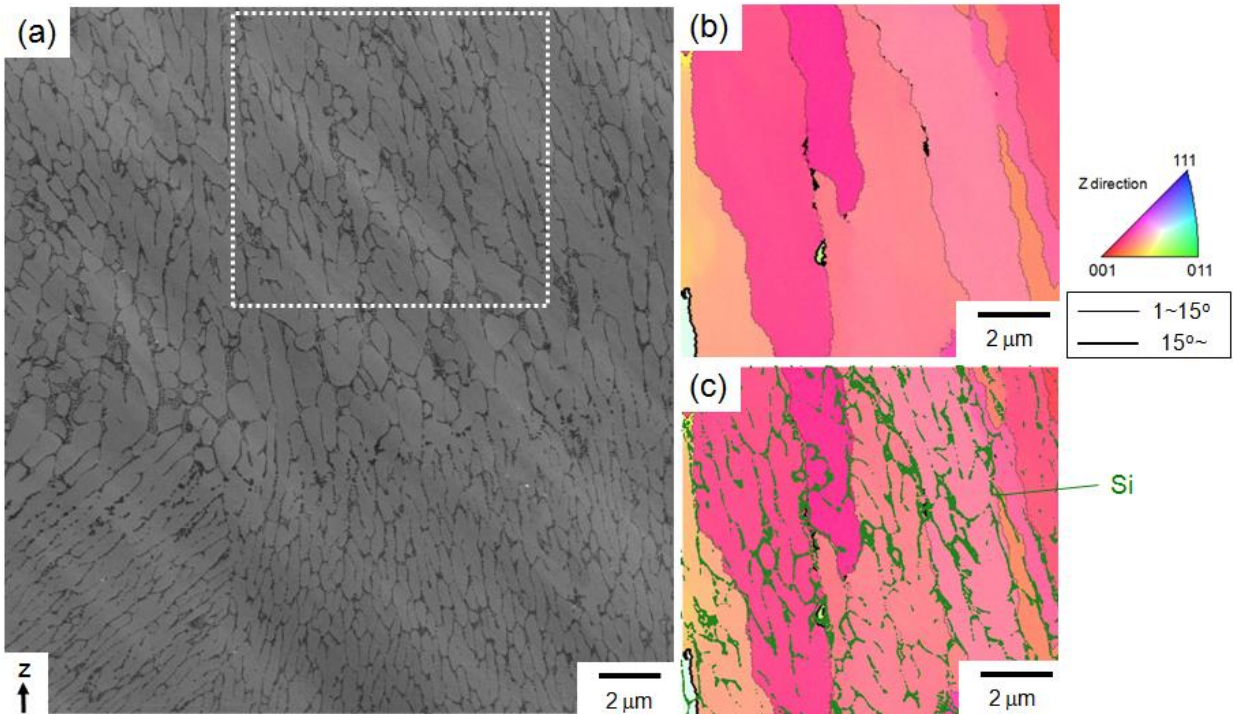


Figure 8 (a) SEM image and (b, c) corresponding orientation color maps (obtained by EBSD analysis) presenting microstructure of as-fabricated AlSi10Mg alloy. In Fig. 9(b), fine lines represent the misorientation (θ) of $1 < \theta < 15^\circ$, while bold lines represent $\theta > 15^\circ$. Green color regions shown in (c) represent the location of Si particles.

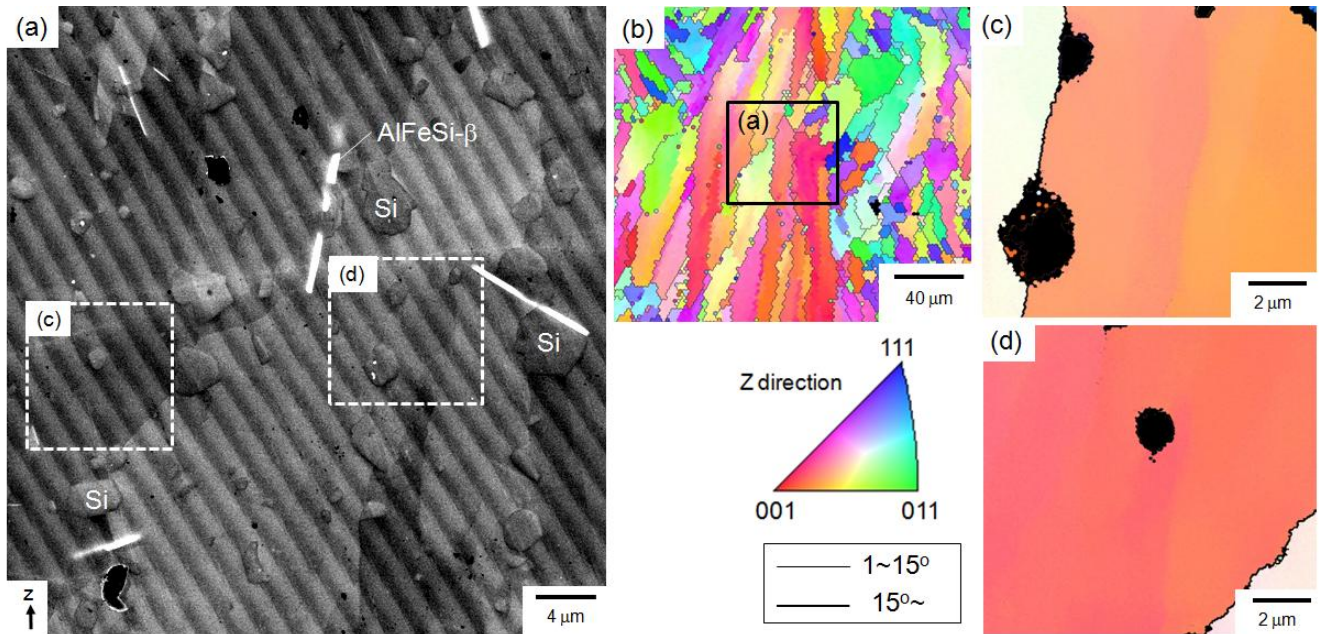


Figure 9 (a) SEM image and (b-d) corresponding orientation color maps (obtained by EBSD analysis) presenting microstructure of the AlSi10Mg alloy solution-treated at 530°C for 6 h. In Fig. 9(b-d), fine lines represent the misorientation (θ) of $1 < \theta < 15^\circ$, while bold lines represent $\theta > 15^\circ$.

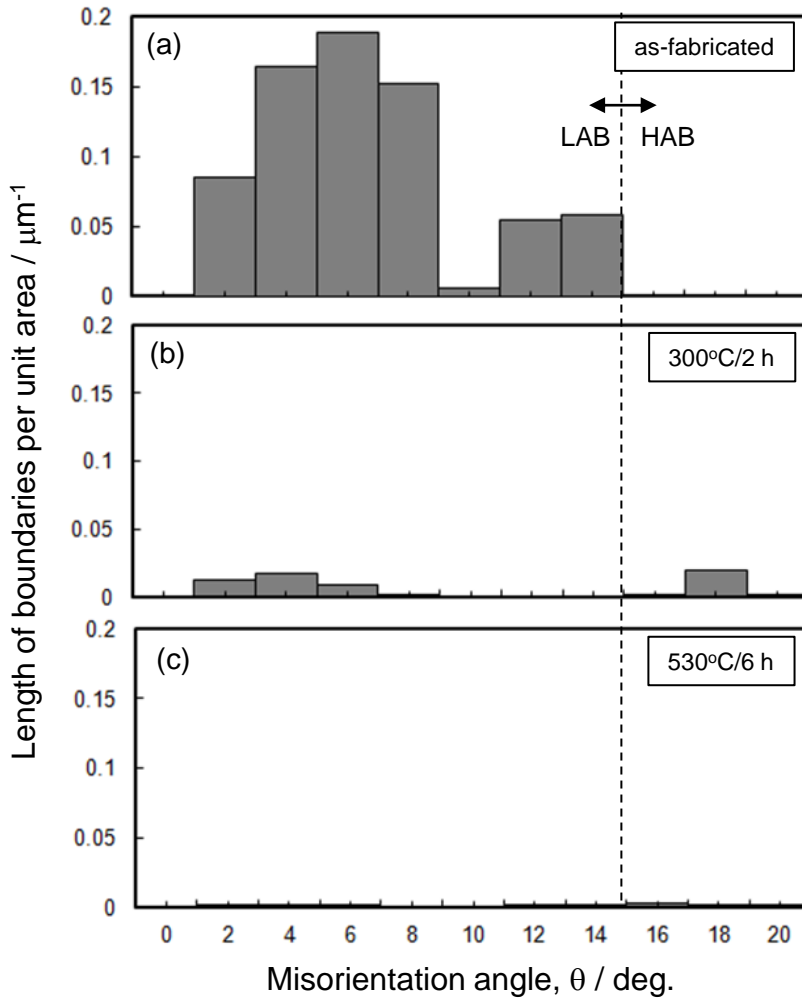


Figure 10 Length of boundaries per unit area as a function of misorientation angle in (a) as-fabricated sample, (b) 300°C/2 h annealed sample, 530°C/6 h heat-treated sample, which were obtained by EBSD analysis at a scanning step size of 0.1 μm .

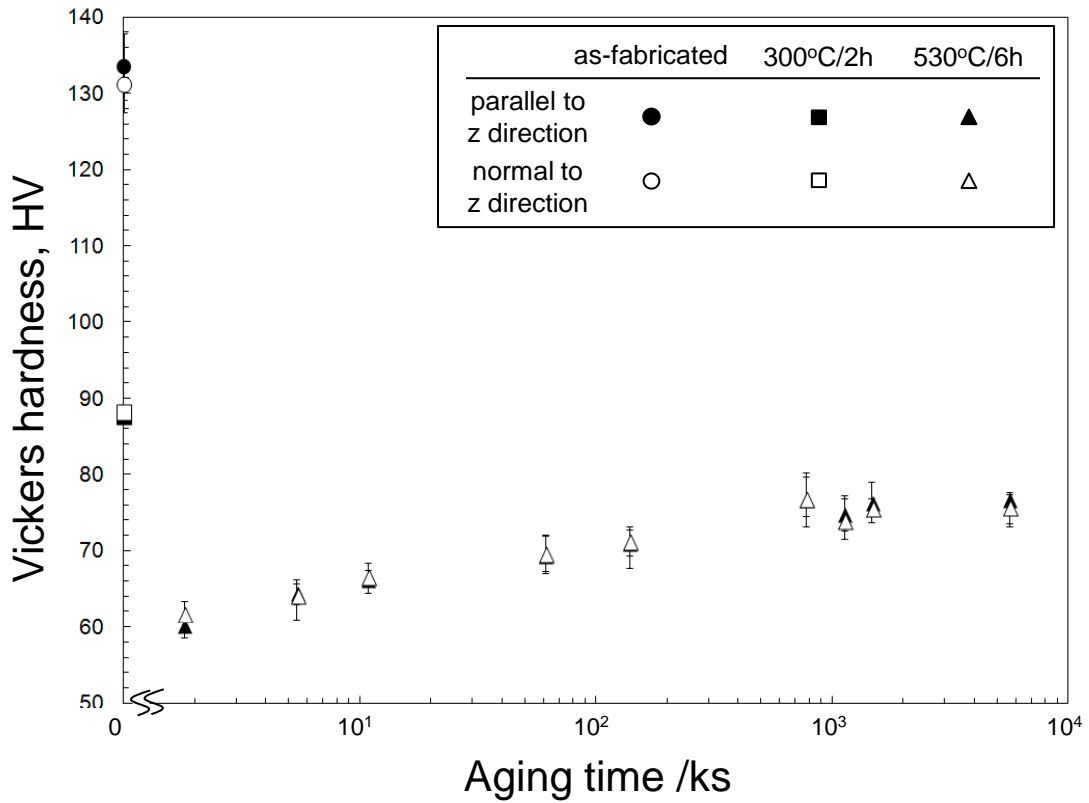


Figure 11 Change in hardness of the solution-treated AlSi10Mg alloy (530°C/6 h) with aging time at room temperature, together with hardness of the as-fabricated sample and the subsequently annealed sample.

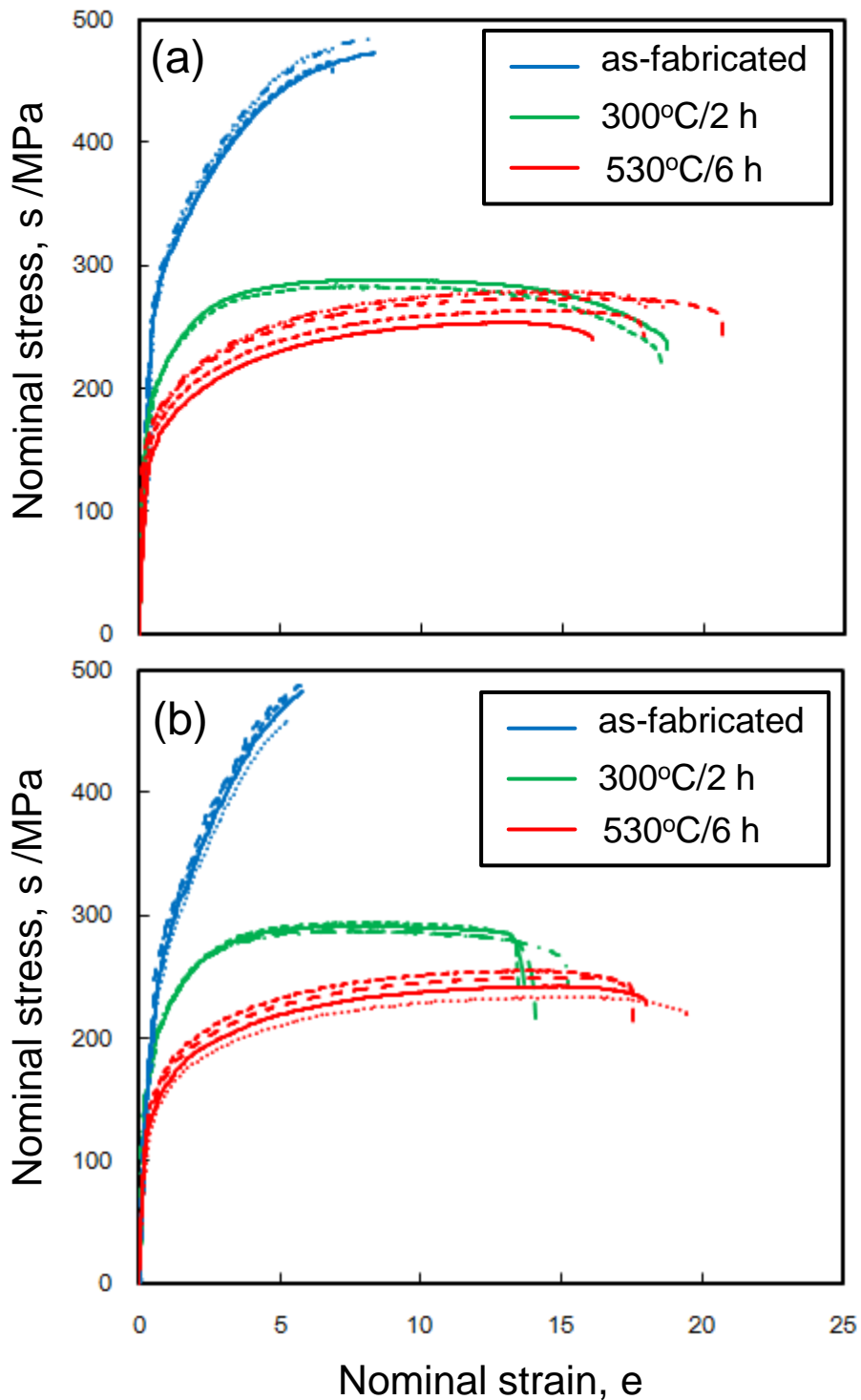


Figure 12 Nominal stress-strain curves of the AlSi10Mg specimens measured by tensile tests at room temperature: (a) tensile direction normal to Z direction, (b) tensile direction parallel to Z direction.

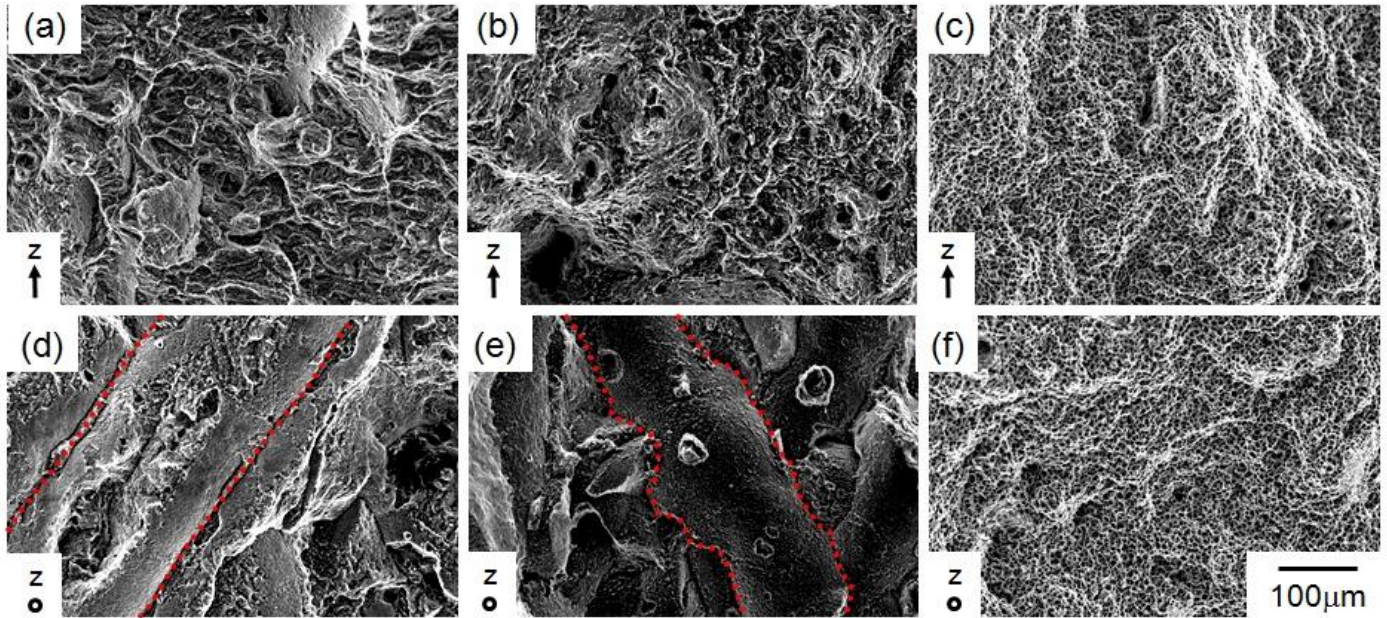


Figure 13 Fracture surfaces of (a, d) the as-fabricated specimen, (b, e) the annealed specimen (300°C/2 h) and (c, f) solution -treated specimen (530°C/6 h) : (a-c) tensile direction normal to Z direction, (d-f) tensile direction parallel to Z direction.

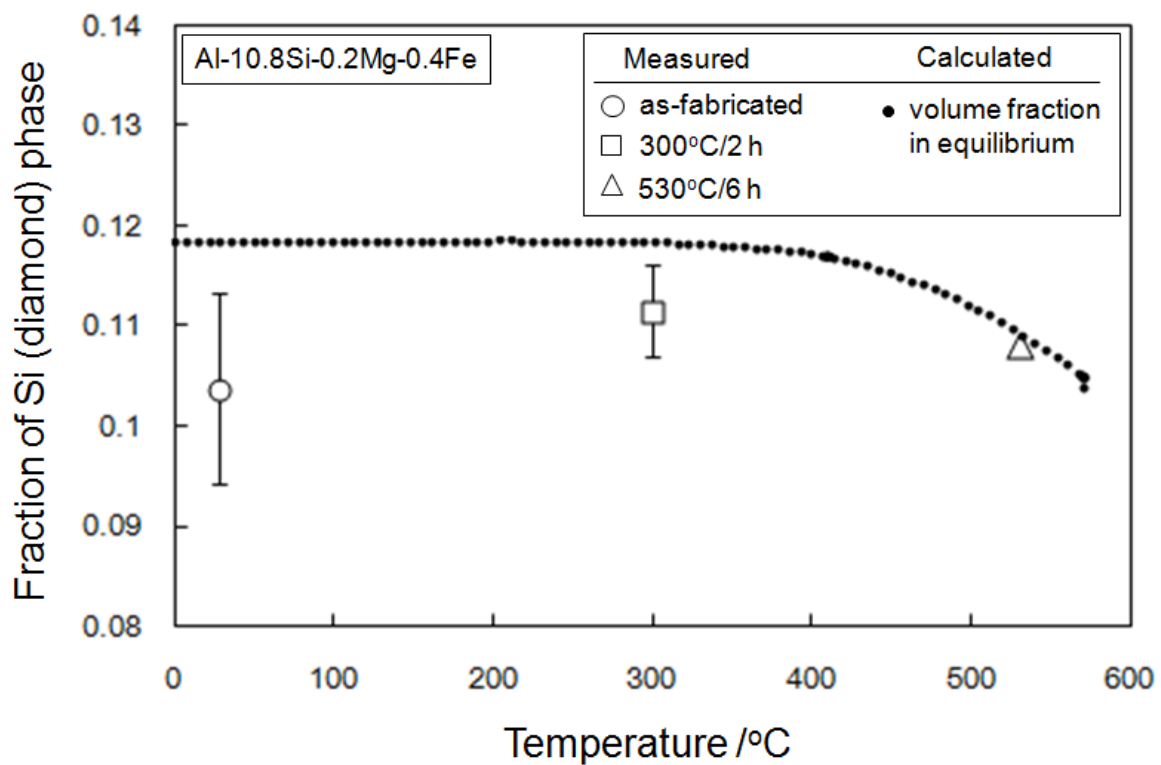


Figure 14 Experimentally measured area fractions of Si particles in studied samples as a function of heat treatment temperature, together with calculated volume fraction of studied composition in equilibrium.

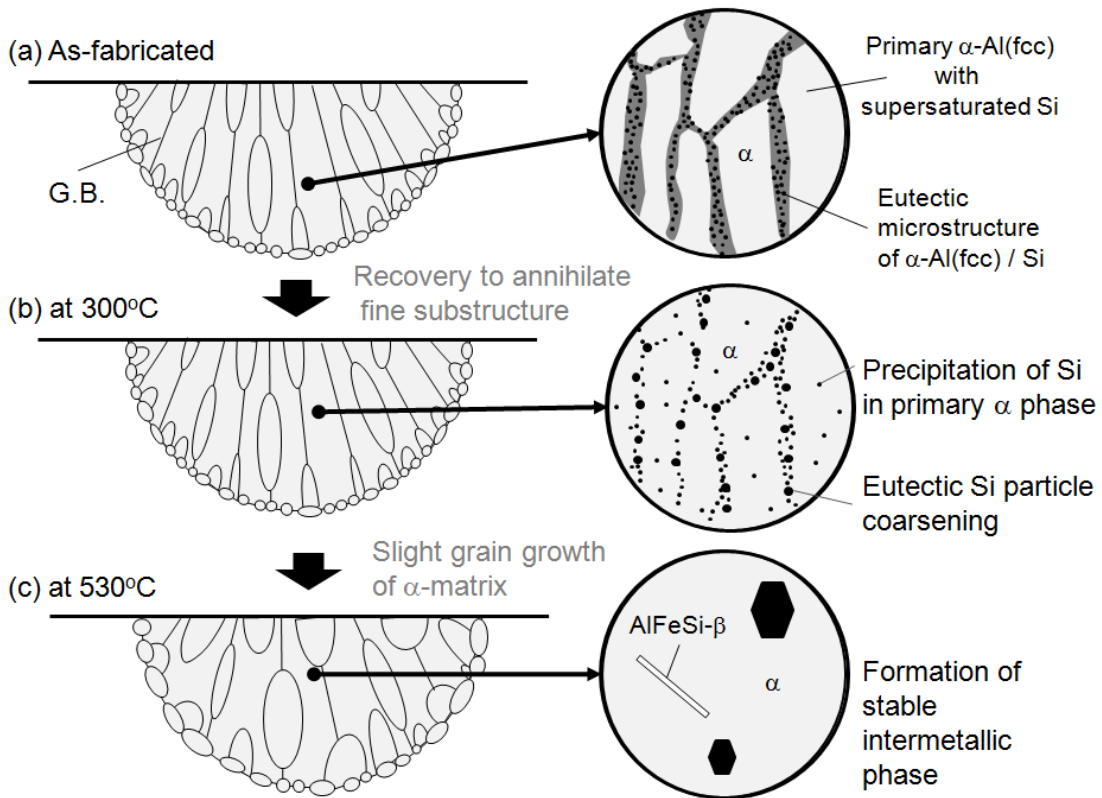


Figure 15 Schematic showing change in microstructure of selectively laser-melted AlSi10Mg alloy, as a result of heat treatment.

Table 1 Chemical composition of studied AlSi10Mg alloy (wt%)

		Si	Fe	Cu	Mn	Mg	Ni	Zn	Pb	Sn	Ti
nominal		9.0 ~ 11.0	≤ 0.55	≤ 0.05	≤ 0.45	0.20 ~ 0.45	≤ 0.05	≤ 0.10	≤ 0.05	≤ 0.05	≤ 0.15
ICP analyzed	powder	10.73	0.42	-	-	0.17	-	-	-	-	-
	as-built	10.77	0.40	-	-	0.18	-	-	-	-	-

Table 2 Microstructural parameters of AlSi10Mg alloy specimens fabricated by selective laser melting and subsequently heat-treated at different temperatures

		As-fabricated	Annealed at 300°C for 2 h	Solution treated at 530°C for 6 h	
α -Al matrix	EBSD analysis with a step size of 2 μm	Area fraction of [001] oriented region along z direction	0.20	0.17	0.17
		Length of high angle boundaries per unit area (μm^{-1})	0.26	0.26	0.23
		Mean spacing of high angle boundaries, d_{HAB} (μm)	7.6	7.6	8.6
Si particles	SEM image analysis	Average area fraction	0.103	0.112	0.108
		Number density (μm^{-2})	-	16.3	0.03
		Mean particle size (μm)	-	0.08	1.80

Table 3 Tensile properties of the AlSi10Mg alloy specimens fabricated by selective laser melting and subsequently heat-treated at different temperatures.

Tensile direction	0.2% proof stress / MPa		Tensile strength / MPa		Total elongation / %	
	X/Y direction	Z direction	X/Y direction	Z direction	X/Y direction	Z direction
As-fabricated	279	220	475	476	7.5	5.5
Annealed at 300°C for 2 h	180	175	285	290	18.6	14.2
Solution treated at 530°C for 6 h	153	139	269	245	18.3	18.1